Reservoir Simulation with the Finite Element Method Using Biot Poroelastic Approach

Yibing Zheng, Robert Burridge and Daniel Burns
Earth Resources Laboratory
Dept. of Earth, Atmospheric, and Planetary Sciences
Massachusetts Institute of Technology
Cambridge, MA 02139

Abstract

We are developing a finite element program for oil and gas reservoir simulation based on Biot's poroelastic theory, where a simultaneous solution is sought for both the pore pressure and strain in the solid phase. Several 2-D and 3-D cases are presented, which are compared with analytical solutions for verification of this approach. We have also applied this method to simulate surface subsidence due to gas and oil production in a subsurface reservoir. The development of this code is still in its initial stage, but the approach shows promise.

1 Introduction

Oil reservoir simulation serves an important role in forecasting oil production, understanding surface subsidence, predicting strain and stress development in the oil field, and preventing well damage. Oil reservoirs are composed by porous media, which include both a solid phase and pore spaces filled with oil, gas and water. The pore pressure and the strain in the solid matrix have instant interaction between each other. Any change of the pore pressure or the depletion of fluid volume will affect the strain of the solid, or vice versa. Biot (1941) developed the first three-dimensional coupled poroelastic system to describe the dynamics of porous media with the coupling between the fluid flow and the stress. This pioneer work is a basic isothermal theory with saturated single phase flow inside solid matrix, which is based on a linear stress-stain constitutive relationship and a linear form of Darcy's flow law. Our reservoir simulation program stems from this Biot's coupled system.

In reservoir simulation, in order to solve the above differential system, the finite element and finite difference methods are the two most commonly used techniques. The finite difference method is simple and easy to implement. However, the finite element method is becoming more and more popular in reservoir simulation, partly due to its flexibility in dealing with boundaries. The element shape is not required to be square so that the element mesh can handle a very complex geometry.

In this report, we apply the finite element method to solve the fully coupled geodynamic system. We will first introduce the basic theory and the finite element formulation. Then the structure and the functions of the program will be discussed. Several 2-D and 3-D simple models are presented for its verification by comparison with analytical solutions. Large scale reservoir models with fluid production are simulated with the program.

2 Theory and FEM Formulation

Biot's poroelastic theory (Biot, 1941, 1955) includes a stress-strain constitutive equation and a fluid mass balance equation. It can be written in vector and tensor notations as

$$\mathbf{T} = \mathbf{c} : \varepsilon - \alpha \mathbf{I} p, \tag{1}$$

$$\zeta = \alpha \nabla \cdot \mathbf{u} + \frac{p}{\mathrm{M}}, \tag{2}$$

where $\mathbf{T}$ is the total stress, $\mathbf{c}$ is the elasticity tensor of the solid matrix, ε is the strain tensor, p is the pore pressure, $\mathbf{I}$ is the identity matrix, and α is the Biot's constant representing the coupling between the stress and the pore pressure. In the second equation, ζ is the increment of fluid content, $\mathbf{u}$ is the displacement of the solid matrix, and 1/M is the specific storage coefficient at constant strain, which is related to the compressibilities of the fluid and solid phases. When both the solid and the fluid are assumed compressible, the coefficient 1/M is defined by

$$\frac{1}{\mathrm{M}} = \frac{\alpha - n}{K_s} + \frac{n}{K_f}, \tag{3}$$

where n is the material porosity or void number, K_s is the bulk modulus of the solid grain material, and K_f is the bulk modulus of the fluid.

In numerical simulation, we assume the isothermal equilibrium and negligible inertial forces, which means that the equilibrium state is established at all times. Therefore, the force balance equation has the form

$$\nabla \cdot \mathbf{T} + \rho \mathbf{g} = 0 \tag{4}$$

where ρ is the average density, and $\mathbf{g}$ is the gravity. Combining it with Eq. (1) results in

$$\nabla \cdot (\mathbf{c} : \varepsilon) - \alpha \nabla p + \rho \mathbf{g} = 0. \tag{5}$$

For the slow transport of oil, water and gas, Darcy's law is assumed valid, which is

$$\mathbf{q} = -\rho_f \frac{1}{\mu} \mathbf{k} \cdot (\nabla p - \rho_f \mathbf{g}), \tag{6}$$

where $\mathbf{q}$ is the fluid flux, $\mathbf{k}$ is the permeability tensor, μ is the dynamic viscosity, and ρ_f is the density of fluid. The increment of fluid content ζ in Eq. (2) of Biot's theory is basically the fluid volume added into a control volume normalized by this control volume. Therefore, the fluid flux $\mathbf{q}$ and ζ have the following relationship,

$$\frac{\partial \zeta}{\partial t} = -\frac{1}{\rho_f} \nabla \cdot \mathbf{q} = \nabla \cdot \left[\frac{1}{\mu} \mathbf{k} \cdot (\nabla p - \rho_f \mathbf{g}) \right]. \tag{7}$$

By substituting it into Eq. (2), the mass balance equation for fluids becomes

$$\left(\frac{\alpha - n}{K_s} + \frac{n}{K_f}\right) \frac{\partial p}{\partial t} + \alpha \nabla \cdot \frac{\partial \mathbf{u}}{\partial t} + \nabla \cdot \left[\frac{1}{\mu} \mathbf{k} \cdot (-\nabla p + \rho_f \mathbf{g}) \right] = 0. \tag{8}$$

The finite element formulation stems from Eqs. (5) and (8). We choose the solid phase displacement $\mathbf{u}$ and the pore pressure p as the primary variables to be solved simultaneously in the finite element system. The stress and strain can be written in vector form in Cartesian coordinates as

$$\mathbf{T} = \{\tau_{xx}, \tau_{yy}, \tau_{zz}, \tau_{yz}, \tau_{zx}, \tau_{xy}\}^T, \tag{9}$$

$$\varepsilon = \{\varepsilon_{xx}, \varepsilon_{yy}, \varepsilon_{zz}, \varepsilon_{yz}, \varepsilon_{zx}, \varepsilon_{xy}\}^T. \tag{10}$$

Thus the divergence of the stress tensor can be expressed using a differential operator $\mathbf{L}$, as

$$\nabla \cdot \mathbf{T} = \mathbf{L}^T \mathbf{T}, \tag{11}$$

and the strain as

$$\varepsilon = \mathbf{L}\mathbf{u}. \tag{12}$$

From Eq. (1), the stress $\mathbf{T}$ has to be written as

$$\mathbf{T} = \mathbf{c}(\mathbf{L}\mathbf{u}) - \alpha \mathbf{m} p, \tag{13}$$

where $\mathbf{m}$ is a vector as

$$\mathbf{m} = \{1, 1, 1, 0, 0, 0\}^T. \tag{14}$$

In the finite element method, the displacements and pore pressures are expressed using their values at a finite number of points in space (Lewis and Schrefler, 1998). This involves generating elements for the whole space and choosing the interpolation functions to express $\mathbf{u}$ and p with each element in terms of the values at the element nodes. Their expressions with one element are

$$\mathbf{u} = N_u \bar{\mathbf{u}} \tag{15}$$

and

$$p = N_p \bar{\mathbf{p}} \tag{16}$$

where $\bar{\mathbf{u}}$ and $\bar{\mathbf{p}}$ are the vectors of the values of the unknowns at the element nodes. The interpolation functions are matrices N_u and N_p for the displacements and the pore pressures respectively.

Applying the Galerkin method (Zienkiewicz and Taylor, 1989) to Eqs. (5) and (8), the finite element formulation becomes the following linear system for each element (valid only with poroelasticity and low compressibility of fluid):

$$\begin{bmatrix} 0 & 0 \\ Q^T & S \end{bmatrix} \frac{d}{dt} \begin{Bmatrix} \bar{\mathbf{u}} \\ \bar{\mathbf{p}} \end{Bmatrix} + \begin{bmatrix} K & -Q \\ 0 & H \end{bmatrix} \begin{Bmatrix} \bar{\mathbf{u}} \\ \bar{\mathbf{p}} \end{Bmatrix} = \begin{Bmatrix} F_u \\ F_p \end{Bmatrix}, \tag{17}$$

where

$$K = \int_\Omega B^T \mathbf{c} B d\Omega \tag{18}$$

$$B = \mathbf{L} N_u \tag{19}$$

$$Q = \int_\Omega B^T \alpha \mathbf{m} N_p d\Omega \tag{20}$$

$$S = \int_\Omega N_p^T \left(\frac{\alpha - n}{K_s} + \frac{n}{K_f} \right) N_p d\Omega \tag{21}$$

$$H = \int_\Omega (\nabla N_p)^T \frac{\mathbf{k}}{\mu} (\nabla N_p) d\Omega \tag{22}$$

$$F_u = \int_\Omega N_u^T \rho \mathbf{g} d\Omega + \int_\Gamma N_u^T \mathbf{t} d\Gamma \tag{23}$$

$$F_p = \int_\Omega (\nabla N_p)^T \frac{\mathbf{k}}{\mu} \rho_f \mathbf{g} d\Omega - \int_\Gamma N_p^T \frac{q}{\rho_f} d\Gamma. \tag{24}$$

Here, K is the stiffness matrix of the solid phase, Q is the coupling matrix related to Biot's constant α, S is a compressibility matrix related to the bulk modulus of fluid and solid, and H is the permeability matrix. The two right-hand terms, F_u and F_p, are associated with the gravity and boundary conditions. The external loading is represented by $\mathbf{t}$, and q is the mass flow into or out of the element. The local element systems are assembled into a global system.

A symmetric system is usually preferred. Eq. (17) can be converted to a symmetric system by time differentiating the first equation, so that it becomes

$$\begin{bmatrix} -K & Q \\ Q^T & S \end{bmatrix} \frac{d}{dt} \begin{Bmatrix} \bar{\mathbf{u}} \\ \bar{\mathbf{p}} \end{Bmatrix} + \begin{bmatrix} 0 & 0 \\ 0 & H \end{bmatrix} \begin{Bmatrix} \bar{\mathbf{u}} \\ \bar{\mathbf{p}} \end{Bmatrix} = \begin{Bmatrix} -\frac{d}{dt} F_u \\ F_p \end{Bmatrix}. \tag{25}$$

To solve the dynamic problem, the central difference in time is applied to Eq. (25). This yields

$$\begin{bmatrix} -K & Q \\ Q^T & S + H(\Delta t/2) \end{bmatrix} \begin{Bmatrix} \bar{\mathbf{u}} \\ \bar{\mathbf{p}} \end{Bmatrix}_{n+1} = \begin{bmatrix} -K & Q \\ Q^T & S - H(\Delta t/2) \end{bmatrix} \begin{Bmatrix} \bar{\mathbf{u}} \\ \bar{\mathbf{p}} \end{Bmatrix}_n + \Delta t \begin{Bmatrix} -\frac{d}{dt} F_u \\ F_p \end{Bmatrix}. \tag{26}$$

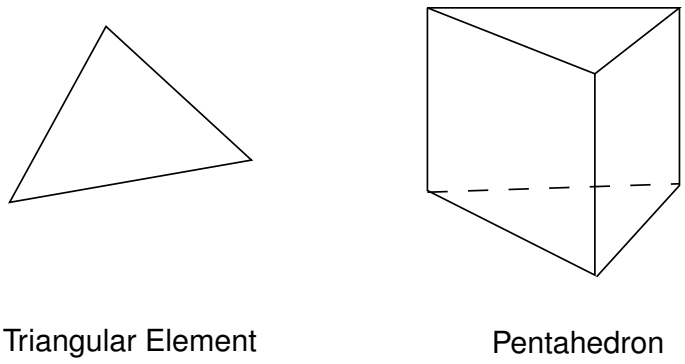

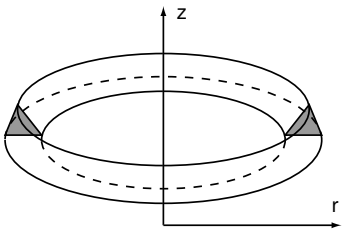

Triangular Ring Element

Figure 1: Elements used in the simulation program

3 The Finite Element Program

The finite element program we developed is based on Eq. (26). It is able to solve coupled poroelastic problems in 2-D, axisymmetric 3-D, and full 3-D.

The program includes three major parts: element subroutine, global matrix assembly, and linear solver. It does not embrace a mesh generation program. For example, a two-dimensional mesh can be generated by the Partial Differential Equation Toolbox in MATLAB.

The element subroutine generates a local element linear system using the specified element shape and interpolation functions, according to Eq. (26). It reads the mesh information from a mesh input file about the coordinates of element nodes and element properties. This is a user-defined subroutine, so that users can write their own code for the desired element shapes and interpolation functions for various applications and geometries. Currently, three element subroutines are included in the program for both 2-D and 3-D simulations. A three-node triangular element code is included for 2-D models. The triangular ring elements or toroids are used for axisymmetric 3-D models. For a full 3-D case, the program utilizes 6-node pentahedrons. Figure 1 shows the shapes of these three elements.

After all the element matrices are obtained, the assembly subroutine assembles them into a global system and stores it in a sparse format. The global assembly code also handles the pressure, force, displacement, and mass flux boundary conditions.

The sparse linear system is then solved by a sparse solver using LU decomposition (Davis, 2003). The solver needs very large memory size, and the condition of the global matrix directly affects its performance. When the global matrix is ill-conditioned, the solver not only requires the most memory, but it also requires a longer time. Furthermore, the solution may not be correct. In order to generate a well conditioned global matrix, the variable units used in the program need to be modified. When ISO units are used, the elasticity constants are of the order of 10^9 Pa (in the stiffness matrix), the Biot constant is between 0 and 1 (in the coupling matrix), and the coefficient $1/M$ is about 10^{-9} Pa^{-1}. These factors cause the ill-conditioned global

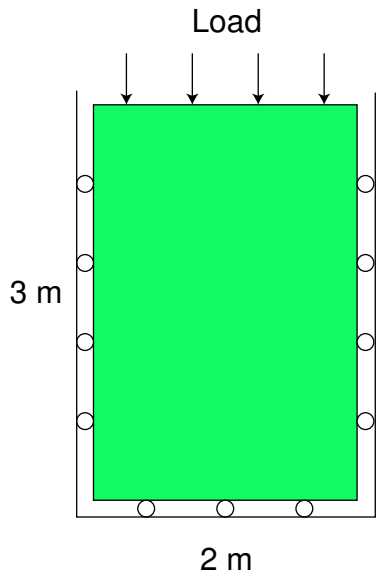

Figure 2: A 2m×3m sample under a load

matrix. Therefore, we use G Pa for pressures and elasticity constants, and 10^9 kilogram for mass.

Currently, we are able to use a computer with 1 GigaByte of memory to simulate a 2-D model with 40,000 nodes.

4 Numerical Experiments

We have done some simple numerical 2-D and 3-D experiments to check the key features of the program by the comparison with analytical solutions.

4.1 Two-Dimensional Small Sample

Consider a 2-D porous sample shown in Figure 2, whose dimensions are 2 m × 3 m, under a uniform undrained loading. The horizontal motions of its left and right boundaries are restricted. The vertical displacement at its bottom is also constrained to zero. Under the undrained condition, fluid is not allowed to flow through the boundaries. The parameters of this sample are listed in Table 1. The applied uniform load is 4 M Pa.

Young's Modulus	1.44×10^4 M Pa
Poisson's Ratio	0.2
Biot's Coefficient, α	0.79
M	1.23×10^4 M Pa
Rock Density	2000 kg/m^3
Oil Density	940 kg/m^3
Porosity	0.2
Permeability	2×10^{-13} m^2
Kinematic Viscosity	1.3×10^{-4} m^2/s

Table 1: List of parameters for the sample shown in Figure 2

From Eq. (26), if Δt, the initial pressure and displacement are all zeros, the linear system becomes

$$\begin{bmatrix} -K & Q \\ Q^T & S \end{bmatrix} \begin{Bmatrix} \bar{\mathbf{u}} \\ \bar{\mathbf{p}} \end{Bmatrix} = \begin{Bmatrix} -F_u \\ 0 \end{Bmatrix}. \tag{27}$$

It is exactly the formulation of the sample under undrained loading. Numerical results of the vertical displacement and pore pressure are shown in Figure 3 to 5, along with the analytical solutions, which lie exactly on top of the numerical results. The pore pressure and the strain are uniform inside the sample. The pore pressure is 1.64 M Pa. The vertical displacement of the solid phase shows a linear function of the height.

Suppose that after the initial undrained loading, the top of the sample is now open so that the pressure becomes zero at the upper boundary, and fluid diffuses and flows freely out through the top. The load remains constant at 4 M Pa. We are studying how the pressure and displacement change with time. The results are plotted in Figures 6 and 7 in different time intervals. When time goes to infinity, the state of this porous sample will settle down at the totally-drained condition, with the pore pressure reaching zero. We are able to compare the result at some initial stage with an analytical solution for an infinite sample, as plotted in Figure 8. The two results agree with each other very well.

The program is able to take gravity into account. A simple example here shows in Figure 9 the static deformation of this sample under gravity. The pore pressure is a linear function of the height (Figure 10), while the vertical displacement of the solid is a quadratic function (Figure 11).

4.2 Surface Subsidence of a 2-D Two-Layer Reservoir Model

Here we are going to simulate a large two-layer reservoir model in 2-D, shown in Figure 12. The lower layer is an oil reservoir with high permeability. The properties of Berea sandstone are used for the lower layer, which are listed in Table 2. However, the upper layer is composed by the material of the same elasticity properties,

Young's Modulus	14.4 G Pa
Poisson's Ratio	0.2
Biot's Coefficient, α	0.79
Rock Density	2100 kg/m^3
Oil Density	940 kg/m^3
Oil Bulk Modulus	2.3 G Pa
Porosity	0.2
Permeability	2×10^{-13} m^2
Permeability of upper layer	2×10^{-17} m^2
Kinematic Viscosity	2×10^{-5} m^2/s

Table 2: List of parameters for the 2-D subsurface reservoir shown in Figure 12

but it has a very low permeability, 10^{-4} times small than that of the lower layer. There is no horizontal motion at either the left or right boundary, and no vertical motion at the bottom. No fluid can flow through the bottom. At the right boundary, we keep the pressure unchanged. Oil is continuously pumped out at a constant rate of 5 mm/hour on the left side of the oil reservoir.

Figure 13 shows the pore pressure distribution inside the two-layer structure after two hours of constant oil pumping. The oil production causes the pressure decrease in the reservoir. Figure 14 shows the continuous decrease of the pore pressure versus time. The pressure is measured at the bottom of the reservoir. The surface subsidence is also calculated as shown in Figure 15 and 16. Figure 15 shows the vertical displacement of the whole structure after two hours of pumping. The surface subsidence versus time is plotted in Figure 16.

4.3 Axisymmetric 3-D Reservoir Model

One special 3-D model is the axisymmetric structure. Our finite element program has an element routine to simulate this kind of reservoir. The following is an example of a two-layer structure, with a well in the

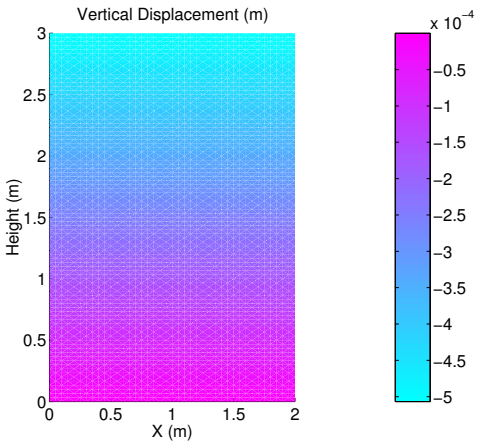

Figure 3: Vertical displacement of the sample under a uniform undrained loading

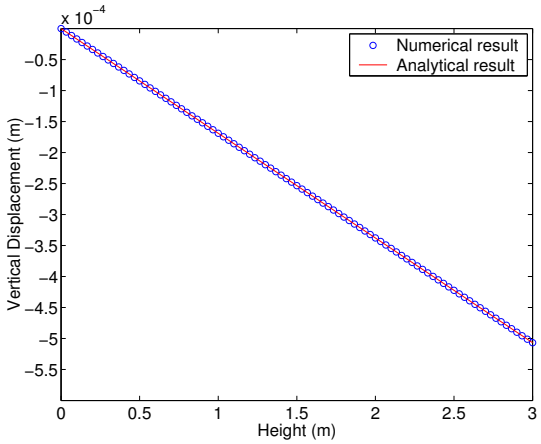

Figure 4: Comparison of the numerical and analytical solutions of the vertical displacement of the sample under undrained loading

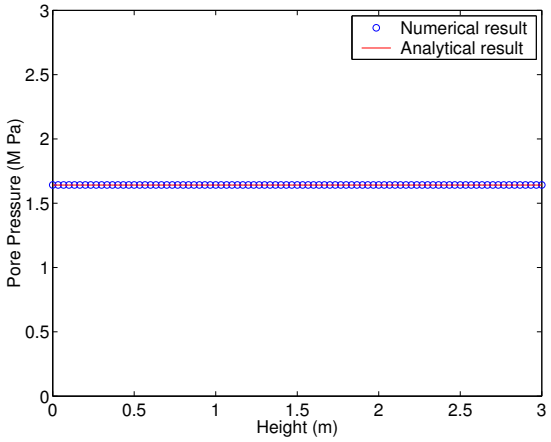

Figure 5: Comparison of the numerical and analytical solutions of the pore pressure of the sample under undrained loading

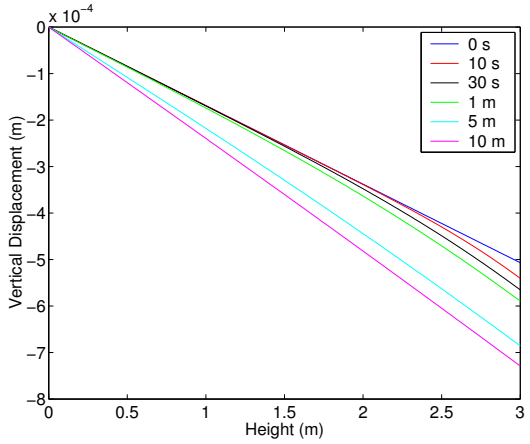

Figure 6: Vertical displacements of the sample after the fluid is allow to freely flow through its top, plotted in different time intervals

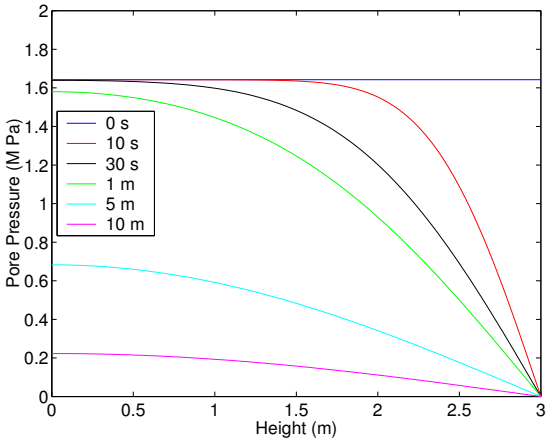

Figure 7: Pore pressures inside the sample after the fluid is allow to freely flow through its top, plotted in different time intervals

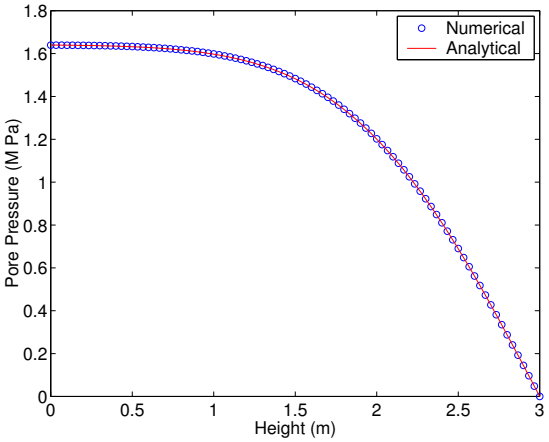

Figure 8: Comparison of the numerical and analytical solutions of the pore pressure of the sample at 30 seconds

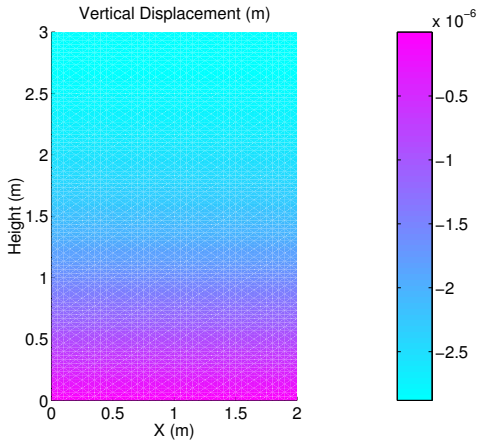

Figure 9: Vertical displacement of the porous sample under gravity

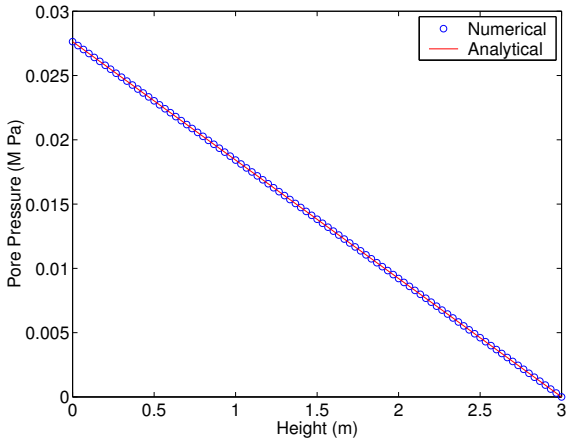

Figure 10: Pore pressures inside the porous sample under gravity is a linear function of the height, compared with the analytical solution.

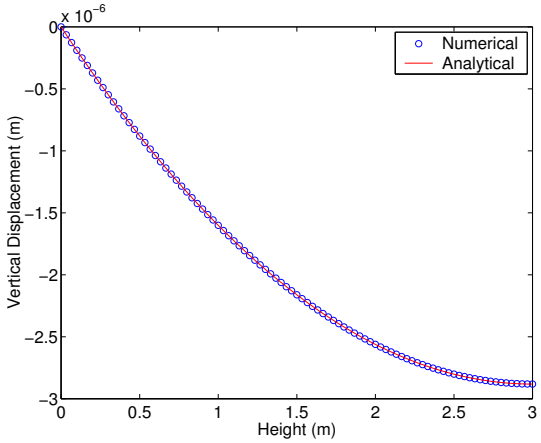

Figure 11: Vertical Displacement of the sample under gravity is a quadratic function of the height, compared with the analytical solution.

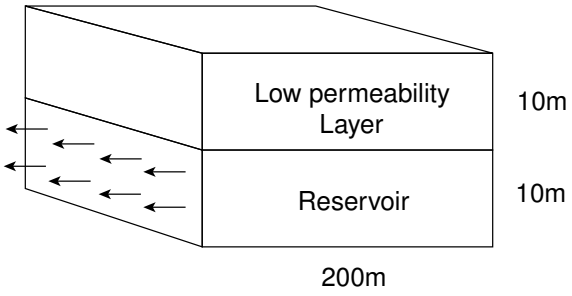

Figure 12: A two-layer model. The lower layer is the reservoir, and the upper layer is non-permeable.

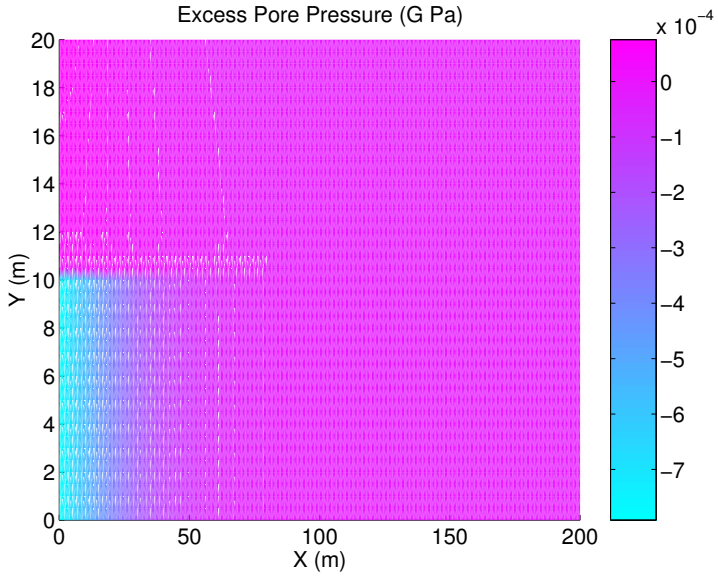

Figure 13: Pore pressure distribution in a two-layer reservoir after two hours of oil pumping

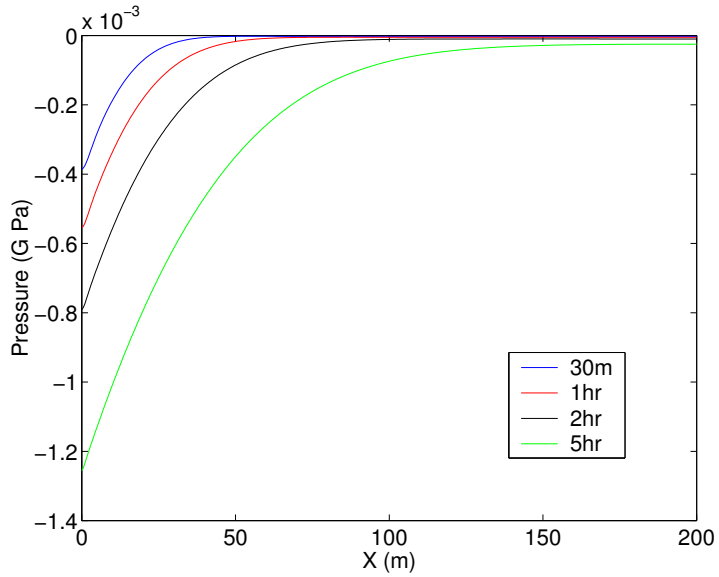

Figure 14: Excess pore pressure change versus time, measured at the bottom of the reservoir

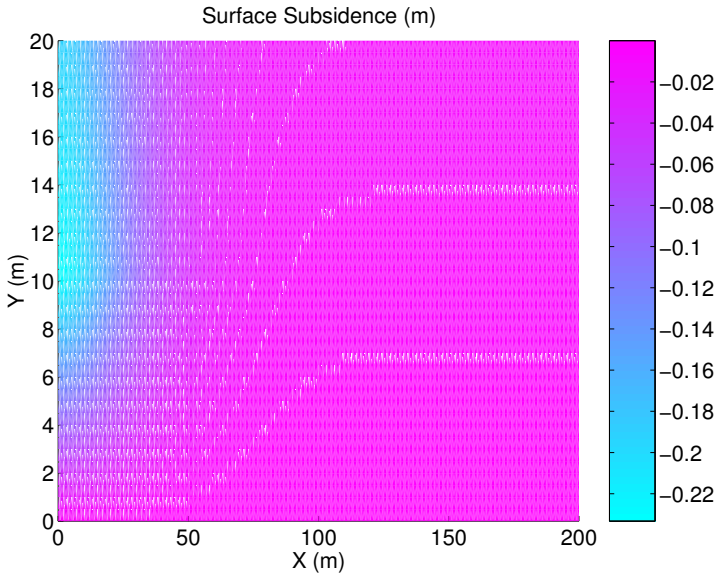

Figure 15: Vertical displacement in a two-layer reservoir after two hours of oil pumping

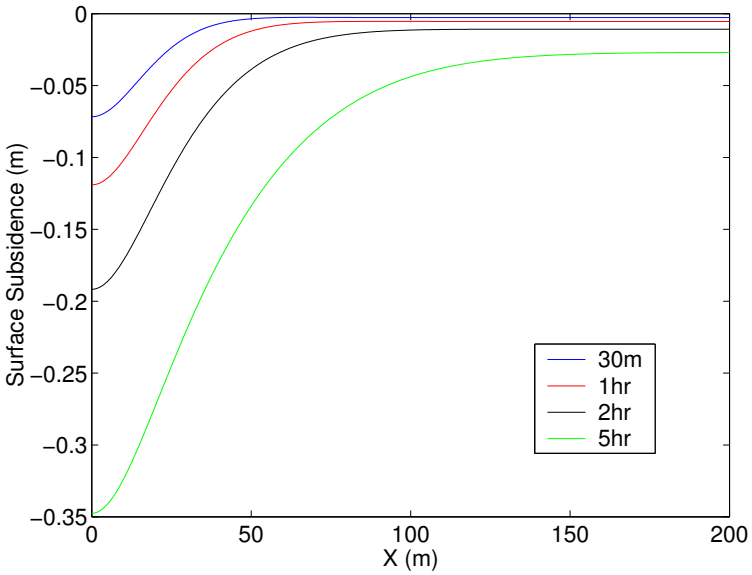

Figure 16: Surface subsidence versus time of a two-layer reservoir with continuous oil pumping

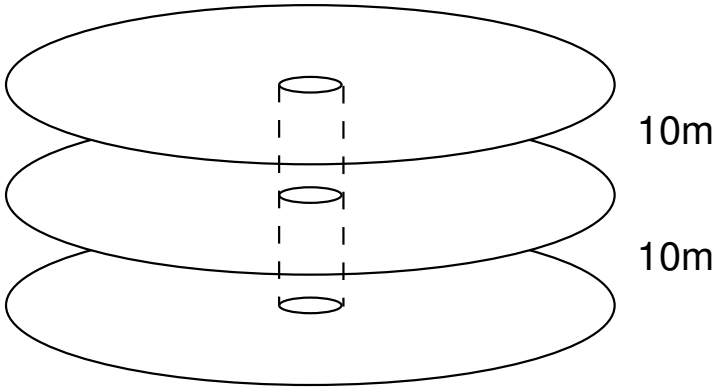

Figure 17: An axisymmetric two-layer reservoir with a production well in the middle

middle. The radius of the well is 0.3 m, and the model radius is about 100 m, as shown in Figure 17. As in the last 2-D model, the lower layer is a oil reservoir with high permeability, while the permeability of the upper layer is 10^{-3} times smaller than that of the reservoir. Other material properties are identical to the previous model. Oil is pumped out from the central well at a constant rate of 5 mm/hour through the wall. There is no fluid flow through the bottom, and the pressure is unchanged at the outer boundary. Horizontal motion of the outer boundary is restricted. In this model, the ring elements of the finite element method are used.

Plotted in Figure 18 is the pore pressure change versus time, measured at the bottom of the reservoir, and the surface subsidence progress is shown in Figure 19 while oil is pumped out at a constant rate.

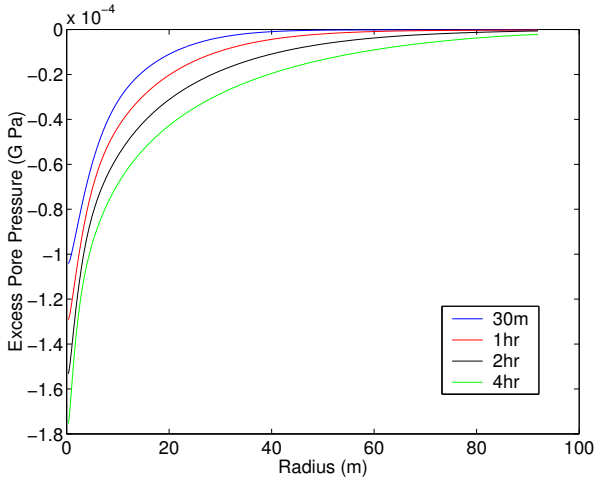

Figure 18: Excess pore pressure at the bottom of an axisymmetric two-layer reservoir versus time, with continuous oil production at its center

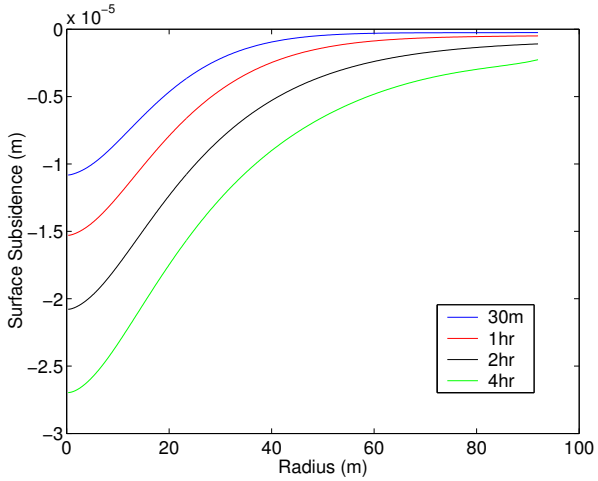

Figure 19: Surface subsidence of an axisymmetric two-layer reservoir versus time, with continuous oil production at its center

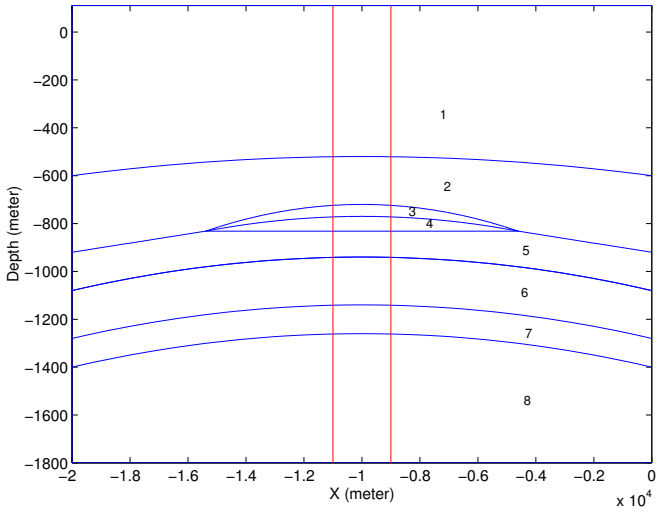

Figure 20: A simplified oil field structure

5 Case Studies

5.1 Surface Subsidence Due to Oil Production

We are now studying a scenario of surface subsidence due to oil production in a subsurface reservoir. The oil reservoir structure is shown in Figure 20, which is a simplified structure representing a complicated real reservoir. It has several slightly dome-shaped layers, labeled 1 to 8 from top to bottom. Their elastic properties are listed in Table 3. Oil is trapped in Layer 3 and 4, where both the permeability and the

Layer	E (M Pa)	Possion's Ratio
1	4500	0.35
2	1100	0.42
3	400	0.25
4	5000	0.20
5	6000	0.20
6	7500	0.20
7	2200	0.40
8	8000	0.30

Table 3: Elastic properties of each layer

porosity are very high. Their permeability is about 300 mD and porosity is around 0.30. Other layers have very low permeability (1 mD). Another important factor is that Layer 3 is a very soft material. Its Young's modulus is only 400 M Pa. When oil is pumped out from the reservoir, Layer 3 will deform the most.

There are many production wells in this oil field, but they mostly cluster at the center. To simulate this oil production problem, we suppose that the well cluster functions as a huge well, whose diameter is 2 km, which is shown in Figure 20 by two vertical red lines. The whole model is also supposed to be axisymmetric. We give a production rate scenario as shown in Figure 21. The production rate increases over the year. After two years of the initial production, the pore pressure and the vertical displacement are shown in Figure 22 and 23, where only the right half of the reservoir is displayed. The left side of these figures represents the center of the field. The major deformation occurs around the central region and above the softest Layer 3. Figure 24 shows the surface subsidence versus time as production continues for ten years.

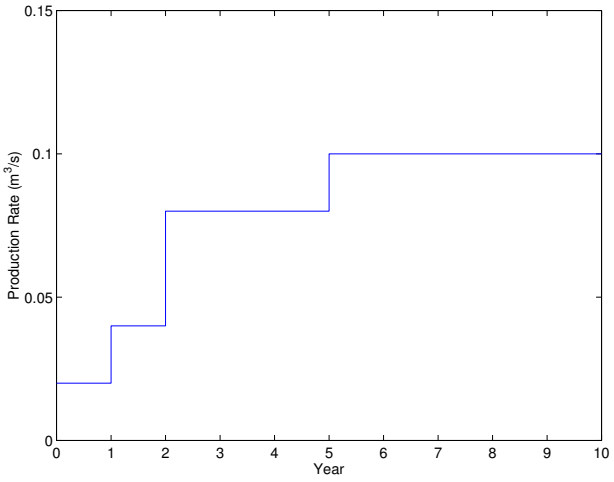

Figure 21: Oil production from reservoir in Layer 3 and 4. The production rate of 0.1 m^3/s is round 54,340 barrels per day.

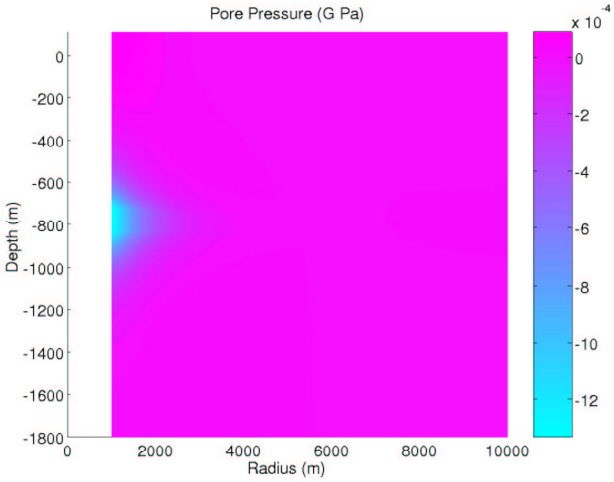

Figure 22: Excess pore pressure after two years of oil production

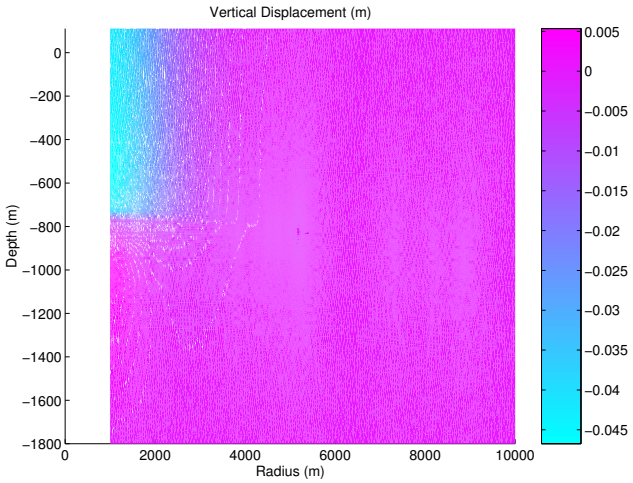

Figure 23: Vertical displacement after two years of oil production

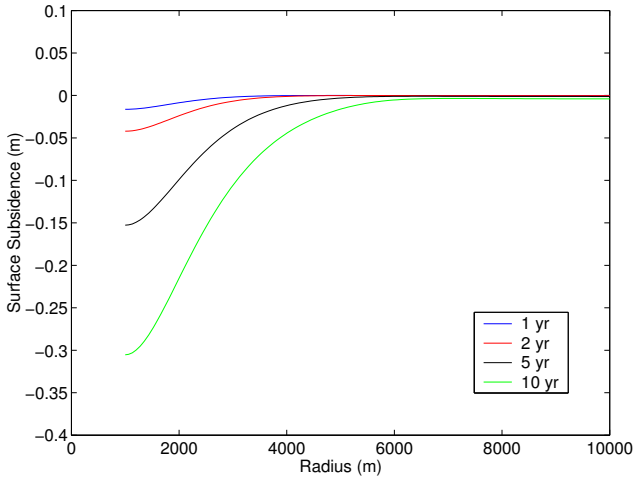

Figure 24: Surface substance versus time over ten years

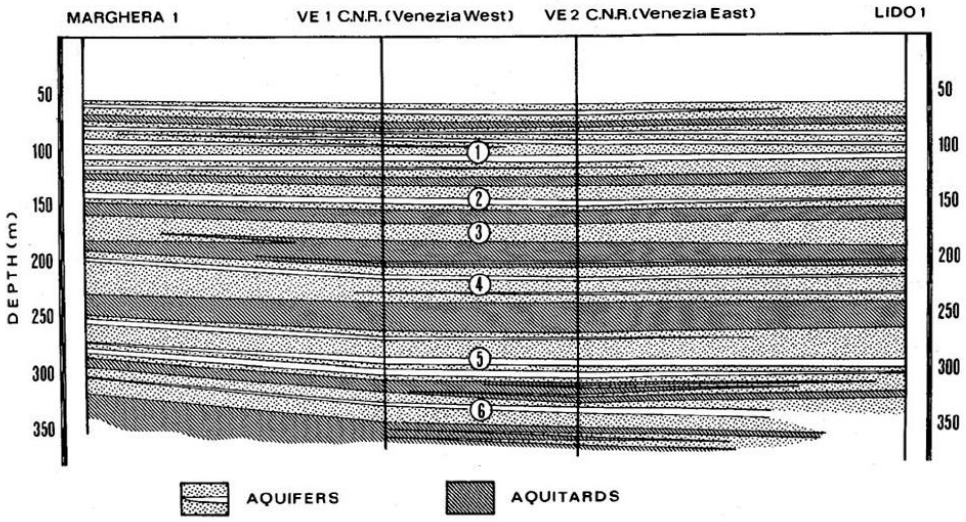

Figure 25: Venice underground structure

5.2 Subsidence of Venice

Background: One of the major factors that contributed to the subsidence of Venice in Italy is the extraction of underground water. A rapid increase in water consumption began around 1930 with the development of the industrial zone of Marghera, which is about 7 km away from Venice.

The subsurface structure of Venice, which contains several horizontal layers, is shown in Figure 25. There are six aquifer layers in all. The sixth aquifer is only exploited in Marghera, so that for the modeling purposes, the sixth aquifer is combined with the fifth. This model was used other authors (Gambolati et al., 1974; Lewis and Schrefler, 1978).

In this simulation, an axisymmetric model is used. Since the wells are clustered in Marghera, they are assumed to act over a circular area of a diameter of 3.0 km. The distribution of wells is modeled by specifying the water flux at a vertical cylindrical surface of a radius of 1.5 km, as shown in Figure 26.

The elastic constants and permeabilities of all layers are listed in Table 4. The Poisson ratios of aquifers and aquitards are assumed to be 0.25 and 0.45, respectively.

	Aquifers		Aquifers	
Layer	E (M Pa)	Permeability (m/day)	E (M Pa)	Permeability (m/day)
1			26.4	0.0432
2	817	13.82		
3			8.6	0.00432
4	817	4.147		
5			9.5	0.000864
6	817	2.765		
7			12.9	0.0138
8	817	5.616		
9			17.3	0.00173
10	817	5.616		

Table 4: Young's modulus and permeability of Venice underground layers

Venice has a good record of the history of total water consumption as shown in Figure 27, as well as the

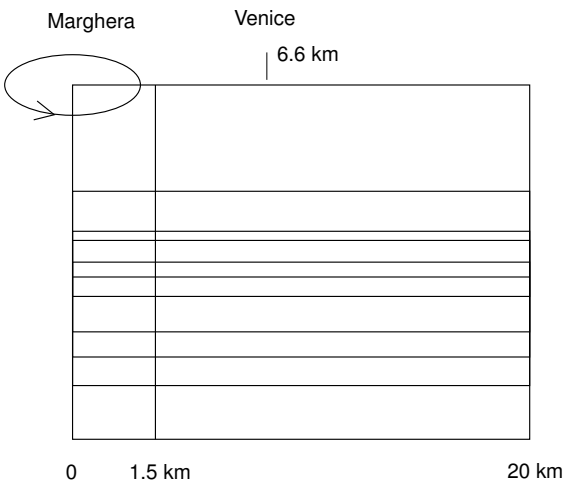

Figure 26: An axisymmetric layered model for simulation of Venice subsidence

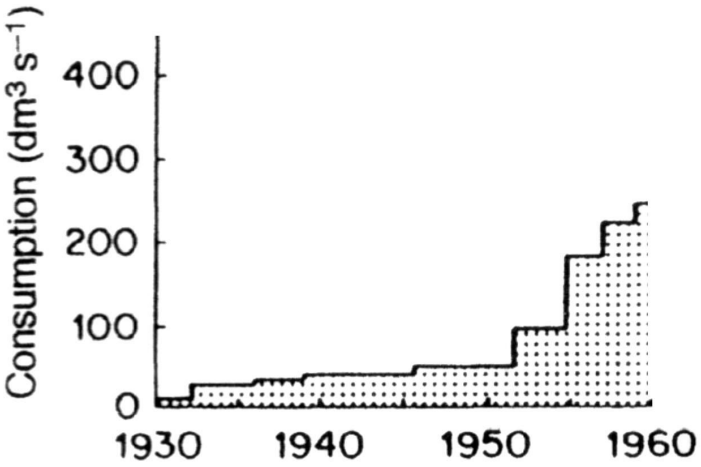

Figure 27: History of water consumption

subdivision of water consumption in the various layers with non-zero extraction rates, as in Table 5.

Figure 28 is the numerical simulation of history of surface subsidence of both Venice and Marghera from 1930 to 1957. The recorded history of subsidence in Venice is also plotted in Figure 29. The numerical modeling agrees very well with the actual history.

6 Conclusions and Future Work

The numerical results from our FE poroelastic program shows that the code is capable of performing various simulations in both 2-D and 3-D. Some results have been compared with analytical solutions, and they show good agreement.

We are still developing the code and adding more features to it. The following functions will be investigated:

1. Non-linear capability. This feature will include the non-linear poroelastic behavior of the solid, as well as the treatment of density and compressibility as functions of pore pressure.

Layer	2	4	6	8	10
1930-1935	43%	7%	21%	29%	0%
1935-1940	22%	7.5%	19%	44%	7.5%
1940-1945	25%	7%	18%	43%	7%
1945-1950	24%	7%	17%	45%	7%
1950-1955	27%	4%	14%	43%	12%
1955-1960	21%	5%	17%	35%	22%

Table 5: Subdivision of water consumption in Venice

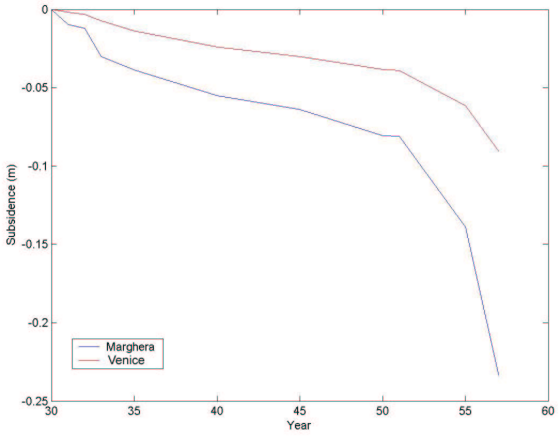

Figure 28: Numerical simulation of Venice subsidence from 1930 to 1957

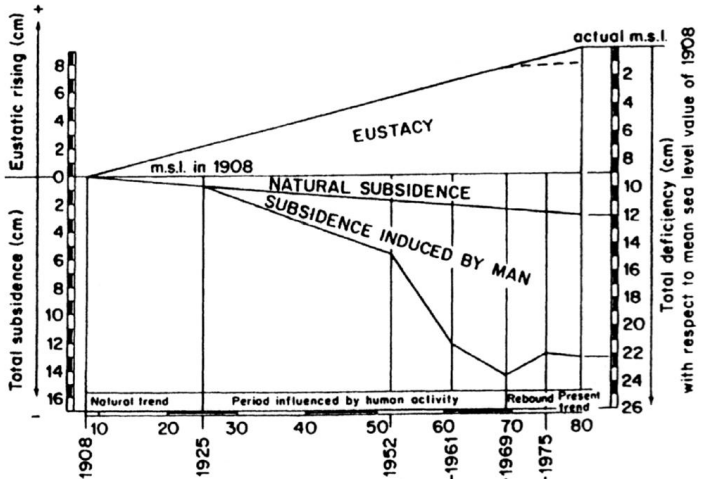

Figure 29: History of water consumption

2. Fractured reservoir simulation.
3. Multiphase flow, which includes oil, water, and gas.

7 Acknowledgments

This work was supported by the Founding Members of the Earth Resources Laboratory at the Massachusetts Institute of Technology.

References

Biot, M. A. (1941). General theory of three-dimensional consolidation. *J. Appl. Phys.*, 12:155–64.

Biot, M. A. (1955). Theory of elasticity and consolidation for a porous anisotropic solid. *J. Appl. Phys.*, 26:182–85.

Davis, T. A. (2003). *UMFPACK Version 4.1 User Guide*.

Gambolati, G., Gatto, P., and Freeze, R. A. (1974). Mathematical simulation of subsidence of venice, 2nd results. *Water Resources Research*, 10(3):563–577.

Lewis, R. W. and Schrefler, B. A. (1978). A fully coupled consolidation model of the subsidence of venice. *Water Resources Research*, 14(2):223–230.

Lewis, R. W. and Schrefler, B. A. (1998). *The Finite Element Method in the Static and Dynamic Deformation and Consolidation of Porous Media*. Wiley, New York.

Zienkiewicz, O. C. and Taylor, R. L. (1989). *The Finite Element Method*, volume 1. McGraw-Hill, London, 4th edition.